Applied Catalysis B: Environmental 103 (2011) 116–127

Contents lists available at ScienceDirect

Applied Catalysis B: Environmental

journal homepage: www.elsevier.com/locate/apcatb

# Displacement reaction of Pt on carbon-supported Ru nanoparticles in hexachloroplatinic acids

Yu-Chi Hsieh[a], Li-Chung Chang[b], Pu-Wei Wu[a,*], Yun-Min Chang[a], Jyh-Fu Lee[c]

[a] Department of Materials Science and Engineering, National Chiao Tung University, Hsin-chu 30010, Taiwan, Republic of China
[b] Graduate Program for Science and Technology of Accelerator Light, Source, National Chiao Tung University, Hsin-chu 30010, Taiwan, Republic of China
[c] National Synchrotron Radiation Research Center, Hsin-chu 30076, Taiwan, Republic of China

ARTICLE INFO

*Article history:*
Received 2 October 2010
Received in revised form 4 December 2010
Accepted 11 January 2011
Available online 15 January 2011

*Keywords:*
Displacement reaction
PtRu bimetallic nanoparticles
Hexachloroplatinic acid
Methanol oxidation
X-ray absorption spectroscopy

ABSTRACT

The displacement reaction of Pt on Ru to form a Ru core and Pt shell (Ru@Pt) bimetallic structure is investigated by immersing the carbon-supported Ru nanoparticles in hexachloroplatinic acids with pH of 1, 2.2, and 8, followed by a hydrogen reduction treatment. Results from inductively coupled plasma mass spectrometry suggest that the dissolution of Ru is mostly caused by the reduction of Pt cations. Images from transmission electron microscopy demonstrate a uniform distribution of Ru@Pt in size of 3–5 nm. Spectra from X-ray absorption near edge structure and extended X-ray absorption fine structure confirm that the pH value of hexachloroplatinic acid determines the type of ligands complexing the Pt cations that affects their activity and consequently the severity of displacement reaction and alloying degree of Ru@Pt nanoparticles. As a result, the samples from pH 1 bath reveal a desirable core–shell structure that displays a reduced onset potential in CO stripping and stable catalytic performance for $H_2$ oxidation while the samples from pH 8 bath indicate the formation of Pt clusters on the Ru surface that leads to poor CO stripping and $H_2$ oxidation characteristics.



## 1. Introduction

The development of bimetallic PtRu nanoparticles has received considerable attention recently because the PtRu not only is an effective electrocatalyst for methanol oxidation reaction (MOR) in direct methanol fuel cells (DMFCs) but also demonstrates impressive CO oxidation ability for reformate hydrogen fuel cells [1–3]. In DMFCs, the oxidation of methanol entails consecutive removals of hydrogen that leaves a CO strongly bonded to the Pt, resulting in a gradual loss of MOR activity. This CO-induced performance degradation is known as CO poisoning which is particularly pronounced in Pt [4–8]. For the reformate hydrogen fuel cells, there is always minute presence of residual CO in the hydrogen feeds so it becomes a concern once the Pt is employed for hydrogen oxidation at the anode. To overcome the CO poisoning effect, the Ru is often alloyed with Pt to facilitate the oxidative removal of CO. It is realized that the Ru can either provide the oxygenated species for CO oxidation to $CO_2$ (bifunctional model) or alter the electronic structure of Pt so the CO–Pt bond strength is weakened considerably (ligand effect) [9–11]. In general, the catalytic performance of PtRu nanoparticles is determined by their size, morphology, crystallinity, composition, as well as the surface distribution of Pt and Ru. Since both Pt and Ru are precious metals, recent researches are steered toward the preparation of PtRu with reduced loading while still maintain desirable catalytic activities.

In general, the atomic arrangement of PtRu nanoparticles can be in alloy or core–shell (core@shell) structure, and both states reveal distinct catalytic performances and life time [12–14]. However, even in an alloyed PtRu there exists possible microsegregation so the Pt/Ru ratio on the surface is different from that of the core. For example, it is reported that the Ru has a larger heat of adsorption for $O_2$ [15,16]. Hence, under an $O_2$ heat treatment, the PtRu surface is enriched with Ru. On the contrary, the Pt exhibits a higher preference for $H_2$ and consequently a $H_2$ treatment engenders a Pt-rich surface instead [15,16]. In contrast, the core–shell structure displays a well-defined regime for the respective core and shell components and the responsible mechanism for the CO oxidation involves the ligand model in which the shell element's electronic structure is altered by the core element underneath. In addition, because the catalytic shell element constitutes a relatively smaller amount as compared to the core element, the effective mass activity can be substantially increased [17–19]. Therefore, the material cost for electrocatalyst is expected to reduce greatly without compromising catalytic ability. To date, a variety of core–shell PtRu nanoparticles have been synthesized and eval-

* Corresponding author at: Department of Materials Science and Engineering, National Chiao Tung University, 1001 University Road, Hsin-chu 300, Taiwan, ROC. Tel.: +886 3 5131227; fax: +886 3 5724727.
*E-mail address:* ppwu@mail.nctu.edu.tw (P.-W. Wu).

0926-3373/$ – see front matter © 2011 Elsevier B.V. All rights reserved.
doi:10.1016/j.apcatb.2011.01.017

uated with various successes. For instance, PtRu deposited on an inexpensive core such as PdCu@PtRu [18] and Co@PtRu [20] are reported with notable performance improvements. Alternatively, the Pt shell is deposited directly on a Ru core with thickness ranging from sub-monolayer to multiple layers forming a Ru@Pt structure [21–23].

To fabricate Ru@Pt nanoparticles, the simplest synthetic scheme entails a displacement reaction which is also known in literature as redox-transmetalation reaction or spontaneous deposition [24,25]. The displacement reaction often occurs in binary systems with constituents revealing distinct values of redox potentials. For example, CuNi, AgGe, and AuGe have been demonstrated and their formation mechanisms are thoroughly discussed [26–28]. In principle, when a binary deposit is in contact with their respective cations in electrolyte, the constituent of lower redox potential is dissolved from the deposit while the one with a higher redox potential is reduced from the electrolyte. Consequently, the deposit on the surface can be tailored for a desirable makeup which is different from that of bulk if the displacement reaction is carefully controlled. Since the Ru exhibits a lower redox potential than that of Pt, once the Ru is immersed in the electrolyte containing Pt cations, the Ru would undergo an oxidation reaction in conjunction with the reduction of Pt cations. Earlier, Brankovic et al. have studied the displacement reaction of $PtCl_6^{2-}$ on both single crystalline and nanoparticulate Ru [29–31]. They suggested that the driving force for the displacement reaction is the potential difference between the $PtCl_6^{2-}$ reduction and $Ru^0$ oxidation. In Ru single crystals, the Ru experiences a surface oxidation reaction forming $Ru(OH)_x$, or even a higher oxidized form. However, they pointed out that the redox potential for the corrosive dissolution of Ru is insufficient to reduce $PtCl_6^{2-}$, so they name this process a cementation reaction as well. In contrast, for Ru nanoparticles, both surface oxidation and corrosion dissolution are likely to provide necessary electrons for $PtCl_6^{2-}$ reduction [29–32]. In addition to Ru, the nature of Pt on the PtRu nanoparticles is still under debate. From X-ray absorption spectroscopy (XAS), Manandhar et al. emphasized that the spontaneously deposited Pt on the Ru core was Pt cations in intermediate oxidation states instead of metallic Pt [29]. However, similar XAS studies by Adzic et al. received different interpretations as they believed that the Pt exists in a metallic state and they attributed the observed d-band vacancy in Pt to the underlying Ru that alters the electronic structure of Pt above [17].

Previously, Spieker et al. adopted the XAS to investigate the hydrolysis reaction of $H_2PtCl_6$ in an aqueous solution and identified the coordination environments of Pt cations in different pHs and $Cl^-$ concentrations [33]. They determined that the $PtCl_6^{2-}$ is present only in an acidic solution with moderate excess of $Cl^-$ or neutral solution with large excess of $Cl^-$. In contrast, the $OH^-$ or $H_2O$ would replace $Cl^-$ as a complexing ligand in alkaline solution with reduced $Cl^-$ content. It is rationalized that the type and number of ligands are critical in determining the activities for the cations. Therefore, any changeup in the number of $H_2O$, $OH^-$, and $Cl^-$ ligand for the Pt cation is expected to affect its redox potential. Consequently, the extent of displacement reaction is likely varied once the Ru is immersed in $PtCl_6^{2-}$ solution at different pHs. This is a variable that is often overlooked by previous studies in PtRu displacement reaction.

In this work, we attempt to distinguish the effect of pH on the Pt complexes for Ru@Pt formation during the displacement reaction. The XAS is employed to provide a qualitative insight on the oxidation states and coordination environments for both Pt and Ru in electrolytes and Ru@Pt nanoparticles. Material characterizations are conducted and correlated with results of CO stripping and $H_2$ oxidation from electrochemical analysis.

## 2. Experimental

### 2.1. Functionalization of commercial carbon black Vulcan XC-72R

Functionalization of commercially available carbon black Vulcan XC-72R (XC72) was conducted by immersing the as-received XC72 in a solution of sulfuric acid (97 wt%) and nitric acid (61 wt%) at a 3:1 volume ratio for 1 h at 25 °C, followed by washing and drying at 80 °C to obtain dry powders. The purpose for this acid treatment was to improve the adhesion of chemically reduced Ru nanoparticles by providing suitable functional groups on the XC72 surface [34].

### 2.2. Fabrication of XC72-supported Ru nanoparticles

Ru nanoparticles were impregnated onto the functionalized XC72 via a chemical reduction method. First, 0.2 g $RuCl_3$ (99.9 wt%) and 0.8 g functionalized XC72 were mixed in excess de-ionized water to form a stable suspension. Subsequently, an appropriate amount of $NaBH_4$, serving as the reducing agent, was dissolved in de-ionized water and slowly added to the $RuCl_3$/XC72 mixture. At this stage, the $Ru^{3+}$ was reduced to form Ru nanoparticles evenly distributed on the XC72 matrix (designated as Ru/XC72). Afterward, the Ru/XC72 was filtered and washed by de-ionized water, followed by 80 °C drying in an oven to remove residual solvent.

### 2.3. Sample preparation of Ru@Pt nanoparticles

To carry out the displacement reaction with Pt cations, the Ru/XC72 powders were deposited on a carbon cloth (CC) of 2 cm × 2 cm which was employed as a substrate. We adopted an ink method in which the ink suspension was composed of 8 mg Ru/XC72, 5 mg PTFE (30 wt%), and 5 mL 99.5 wt% ethanol. The ink suspension was well-dispersed by ultrasonication for 30 min and was transferred to the CC atop a hot plate at 80 °C. After drying out residual solvent, the sample, designated as Ru/XC72/CC, was immersed in 5 mM aqueous solution of hexachloroplatinic acid ($H_2PtCl_6$; 99.9 wt%) at selective pH values. The intrinsic pH value for the 5 mM $H_2PtCl_6$ aqueous solution was 2.2, and it was adjusted to pH 1 by perchloric acid ($HClO_4$) and pH 8 by potassium hydroxide (KOH), respectively. The immersion lasted for 24 h at 40 °C, allowing sufficient replacement of Pt for Ru. The as-prepared samples were thoroughly rinsed with de-ionized water and were designated as "group A". A second set of samples undergoing a hydrogen reduction treatment after the immersion in $H_2PtCl_6$ solution at identical pH conditions was labeled as "group B". The hydrogen reduction was conducted with pure hydrogen at 80 °C for 2 h. Samples after the immersion in $H_2PtCl_6$ solution were designated as Ru@Pt/XC72/CC because the Pt cations were expected to deposit on the Ru nanoparticles forming a Ru core and Pt shell structure. For comparison purposes, we also immersed the Ru/XC72/CC in solutions of $HClO_4$ (pH 1), de-ionized water (pH 7), and KOH (pH 8) to evaluate the chemical stability of Ru/XC72/CC in those solutions and the amount of Ru that was corrosively dissolved. A flow chart for the preparation steps involved is provided in Fig. 1.

### 2.4. Material characterizations

X-ray diffraction (XRD) patterns were obtained by Max Science-M18XHF KXY-8019-1 with a CuKα of 1.54 Å. The X-ray diffractogram was recorded at a scan rate of 4°/min for 2$\theta$ values between 30° and 90°. To distinguish the crystalline state of Ru@Pt, we also carried out XRD analysis for 2$\theta$ values between 36° and 41° at 0.5°/min. Transmission electron microscopy (TEM) was employed to observe the morphology for the as-prepared Ru and Ru@Pt nanoparticles using JEOL JEM-3000F with an accelerating

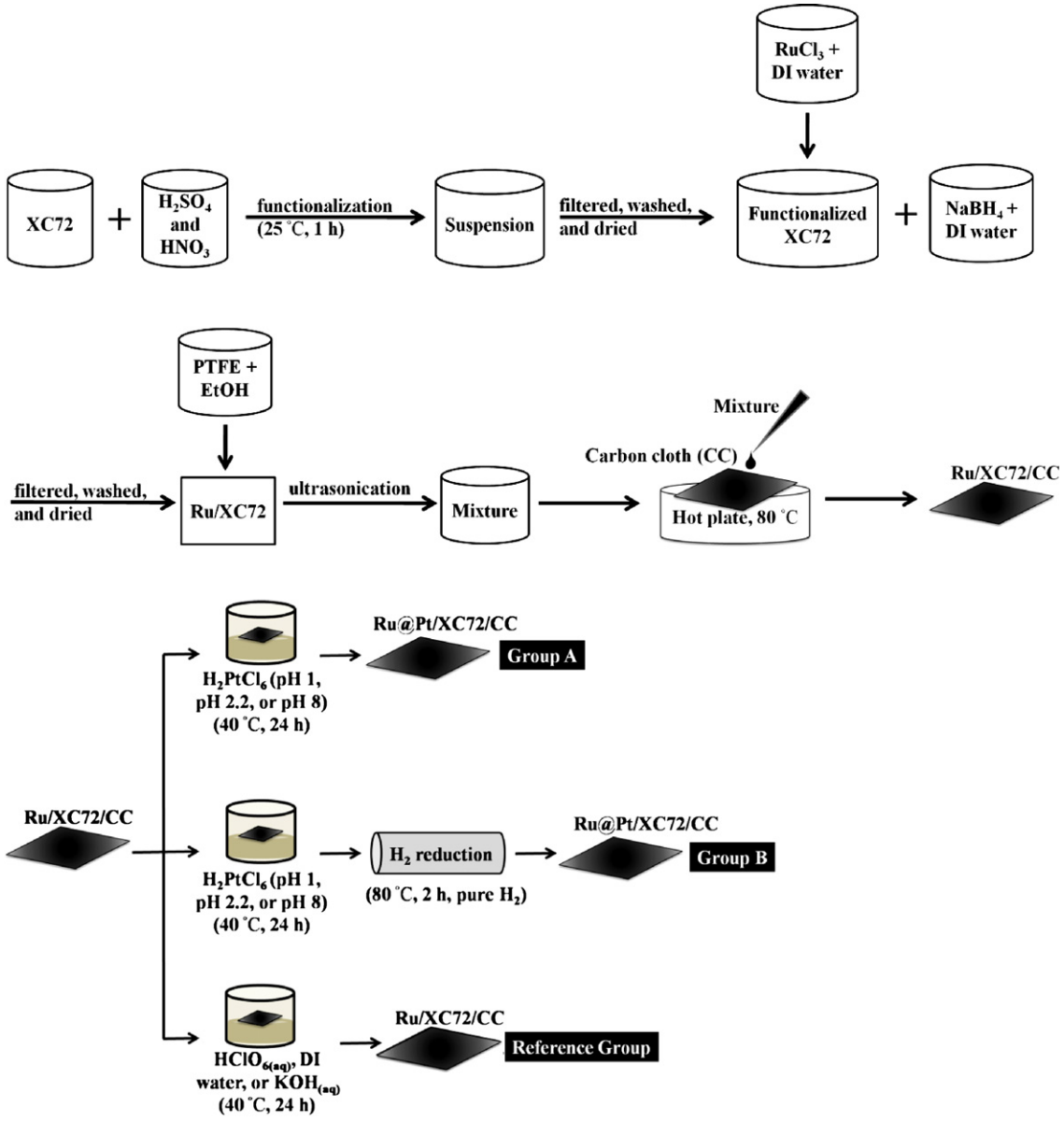


**Fig. 1.** A flow chart for the processing steps involved to prepare samples of group A, group B, and reference group.

voltage of 300 kV. The XC72-supported Ru and Ru@Pt nanoparticles were carefully removed from the CC after rinsing in ethanol followed by ultrasonication. We also obtained the PtRu ratio with an energy-dispersive X-ray spectroscopy (EDX) equipped on the TEM. The exact Pt and Ru amounts for the Pt and Ru@Pt nanoparticles were determined by an inductively coupled plasma mass spectrometry (ICP-MS) where samples of Ru/XC72/CC and Ru@Pt/XC72/CC were dissolved in a solution containing HCl, $HNO_3$, and HF of 2:2:1 volume ratio at 180 °C. In addition, we retrieved liquid samples from the $H_2PtCl_6$ solution after the displacement reaction to validate the concentration of remaining Pt and dissolved Ru cations.

### 2.5. XAS measurements and analysis

X-ray absorption spectra (XAS) for the Pt $L_{III}$-edge (11,564 eV) and Ru K-edge (22,117 eV) were obtained at beamlines BL01C1 and BL17C1 of the Taiwan Light Source, National Synchrotron Radiation Research Center (NSRRC), Hsinchu, Taiwan. The storage ring energy was 1.5 GeV, and the stored current was in the range of 300–360 mA. A double Si (1 1 1) crystal monochromator was adopted for energy selection with a resolution $\Delta E/E$ better than $2 \times 10^{-4}$ at both beamlines. Rh or Pt-coated mirrors were adopted to reject high-order harmonics, collimate (upstream) and refocus (downstream) the X-ray beam. The XAS measurements were conducted in a fluorescence detection mode at 25 °C. A Lytle fluorescence detector along with three gas-filled ionization chambers were used to measure the intensities of the X-ray fluorescence photons from the sample ($I_f$), incident beam ($I_0$), transmitted beam through the sample ($I_t$), and transmitted beam through the reference metal foil or powder ($I_r$). A Pt foil was served as a reference for Pt $L_{III}$-edge measurements and metallic Ru powder was used for Ru K-edge measurements.

Extended X-ray absorption fine structure (EXAFS) data analysis and fitting were processed by IFEFFIT 1.2.11c data analysis package (Athena, Artemis, and FEFF6) [35,36]. In each scan, the recorded data were calibrated by aligning against the reference. After the calibration, they were averaged to achieve better signal quality. X-ray absorption near edge structure (XANES) spectra was acquired after normalization by Athena software. The EXAFS function was obtained by standard protocols including pre-edge and post-edge

background subtraction, and normalization with respect to the edge jump. The detailed procedure has been reported elsewhere [37]. The resulting EXAFS function, $\chi(E)$, was transformed from the energy space to $k$-space. The value $k$ refers to the photoelectron wave vector. At the high $k$-region of $\chi(k)$ data, multiplication by $k^3$ was adopted to compensate the damping of EXAFS oscillations. Next, the $k^3$ weighted $\chi(k)$ data were Fourier-transformed to $r$-space. Specific ranges in $k$-space for the Fourier transformation were selected from 3.32 to 12.74 $Å^{-1}$ for the Pt $L_{III}$-edge and from 4.01 to 13.42 $Å^{-1}$ for the Ru K-edge. The EXAFS curve fitting in $r$-space was applied by a nonlinear least-square algorithm. In addition, the $r$-space ranges for the curve fitting were established without phase correction from 1.29 to 3.12 Å for Pt and from 1.32 to 2.73 Å for Ru. The structural parameters were fitted by Artemis with theoretical standards generated by FEFF6 code [38]. The fitted structural parameters included the coordination number ($N$), bond distance ($R$), Debye–Waller factor ($\Delta\sigma_j^2$), and inner potential shift ($\Delta E_0$). Two assumptions were made in the EXAFS fitting for the $H_2PtCl_6$ solution. First, we assumed that the Pt cation (IV) complexes were octahedrally coordinated, which kept the sum of Pt–Cl and Pt–O coordination number at six for all complexes. Second, the difference in $\Delta\sigma_j^2$ for the Pt–Cl and Pt–O was assumed to be identical [33]. In addition, the amplitude reduction factor ($S_0^2$) for Ru was obtained by analyzing the reference Ru powder and found to be 0.79.

## 3. Results and discussion

### 3.1. Material characterizations on Ru@Pt/XC72/CC

The XRD patterns are able to provide qualitative evidences for the PtRu displacement reaction since the Pt and Ru adopt distinctive lattices of fcc and hcp, and the alloying of a relatively larger Pt atom (1.35 Å) into Ru (1.3 Å) structure is expected to render a slight expansion in the lattice parameter. Fig. 2(a) exhibits the XRD patterns for the XC72/CC, Ru/XC72, Ru/XC72/CC, and group A of Ru@Pt/XC72/CC from $H_2PtCl_6$ solution of pH 1, pH 2.2, and pH 8, respectively. As shown, the XC72/CC exhibited an amorphous background with a notable diffraction peak at 43.62°. This peak was also present for remaining samples in Fig. 2(a) and it is a characteristic carbon signal as evidenced by many studies [39–42]. For the Ru/XC72, the hcp phase of Ru was confirmed with relevant planes properly indexed. In addition, the XRD pattern suggested a polycrystalline nature with relative intensity consistent with that of JCPDS 06-0663. The observed strong signals for the Ru/XC72 over those of Ru/XC72/CC were attributed to the sample preparation difference where a larger amount of Ru/XC72 was used for the XRD measurement. For samples of Ru@Pt/XC72/CC, the only discernible diffraction peaks were (1 0 0) and (1 0 1) which were associated with the Ru lattice. Since the (1 0 1) overlapped with the background diffraction from the XC72 and CC, we repeated the XRD measurements at a slower scan rate around the (1 0 0) peak for comparison. The high-resolution XRD pattern for 36°–41° is displayed in Fig. 2(b). As shown, the Ru/XC72/CC revealed a (1 0 0) peak at 38.74°. For samples of pH 1, pH 2.2, and pH 8, the (1 0 0) peak was located at 38.7°, 38.5°, and 38.82°, respectively. The minor variation between these diffraction peaks was likely caused by poor crystallinity of Ru after displacement reaction as well as background noises from the XC72 and CC that compromised signal quality considerably. We believed that the possibility for PtRu alloying was rather remote as the displacement reaction took place at 40 °C and any interdiffusion between Pt and Ru was negligible. Hence, the formation of a quasi-core–shell Ru@Pt was presumed because from the standpoint of displacement reaction, the Pt was deposited upon removal of Ru and this dislocation process was occurring on

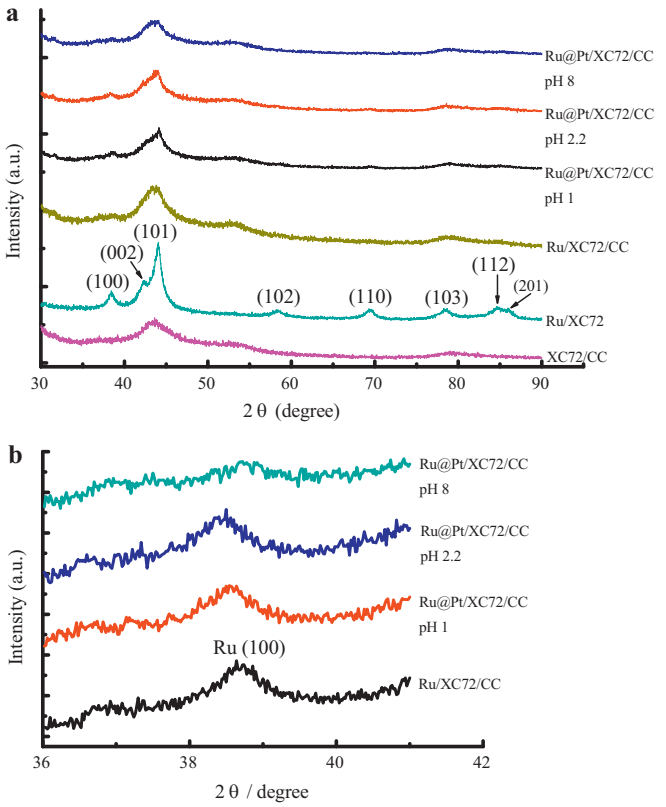


**Fig. 2.** The XRD patterns for the XC72/CC, Ru/XC72, Ru/XC72/CC, and Ru@Pt/XC72/CC from group A of pH 1, pH 2.2, and pH 8 in scan range of (a) 30°–90° and (b) 36°–42°.

the Ru surface exclusively. According to Alayoglu et al., for Ru@Pt nanoparticles with an approximately 1–2 monolayer-thick Pt shell, both hcp Ru and fcc Pt diffraction peaks were observed, albeit with considerable noises and reduced crystallinity [14]. In our case, unfortunately, the Pt signal was not identified form Fig. 2(b). Earlier, Manandhar and Kelber studied the spontaneous deposition of Pt on Ru single crystals by X-ray photoelectron spectroscopy and confirmed that the Pt was partially reduced as Pt(II) cations on the Ru surface [29]. Therefore, it is likely that the Pt might exist in an oxidized form instead of metallic one in our case after the displacement reaction.

To validate our premise that the Pt was not present in metallic state after the displacement reaction, we carried out the hydrogen reduction treatment and Fig. 3(a) demonstrates the XRD patterns for Ru@Pt/XC72/CC from samples of group B. Similar to what we observed in Fig. 2(a), a broad diffraction peak was recorded around 44° which was attributed to the combined effects of XC72/CC and Ru (1 0 1). Fig. 3(b) provides the high-resolution XRD pattern for 36°–42°. For samples of pH 1, pH 2.2, and pH 8, the Ru (1 0 0) peak was located at 38.5°, 38.54°, and 38.62°, respectively. These peaks were orderly shifted to lower angles as compared to that of Ru/XC72/CC at 38.74°. This suggested a moderate alloying of Pt in Ru matrix after the hydrogen reduction treatment. In addition, the degree of alloying increased with baths at smaller pH value. Moreover, for samples of pH 2.2 and pH 8, there appeared a minor diffraction peak of Pt (1 1 1) at 39.48° corresponding to a fcc Pt with a lattice parameter of 3.95 Å. This value was slightly larger than the bulk Pt of 3.92 Å which was unexpected because the underlying Ru core is presumed to exert finite constrains for the Pt lattice above, causing it to shrink its lattice parameter slightly. However, we rationalized that the signals from CC and XC72 might interfere with diffraction responses from the Pt so the peak location might

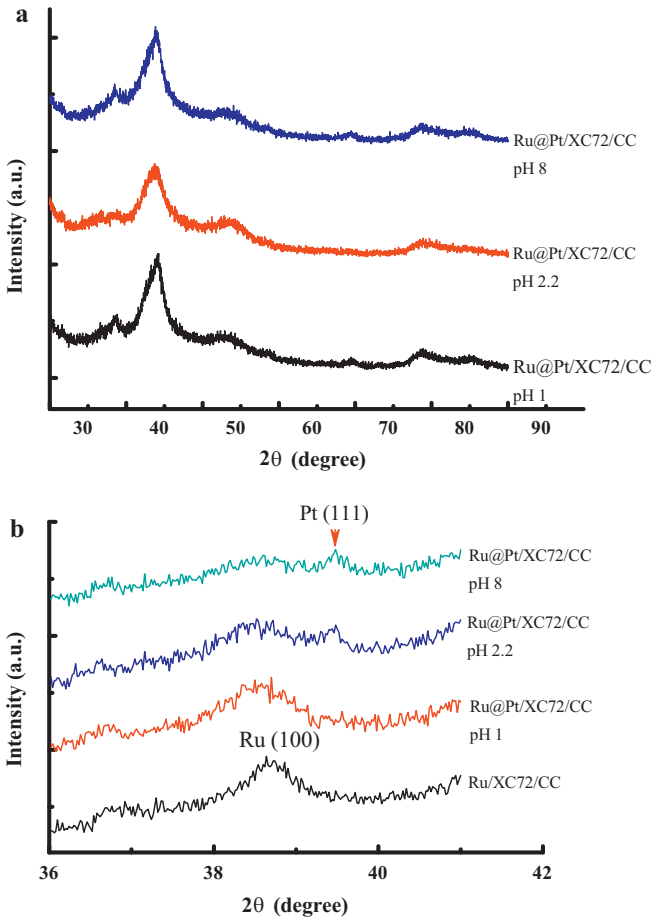


**Fig. 3.** The XRD patterns for the Ru@Pt/XC72/CC from group B of pH 1, pH 2.2, and pH 8 in scan range of (a) 30°–90° and (b) 36°–42°.

lose its fidelity. Nevertheless, we concluded that the Pt was present initially in some oxidized forms but transformed to metallic one after the hydrogen reduction treatment.

The TEM images for Ru/XC72 and Ru@Pt/XC72 (group A) of pH 1, pH 2.2, and pH 8 are exhibited in Fig. 4. Also displayed in the insets are their respective pictures in high magnification. As shown in Fig. 4(a), the Ru nanoparticles were irregular but uniformly distributed in the XC72 support with an average size of 3.6 nm. The high-resolution image confirmed a polycrystalline structure for each individual particle. Interestingly, their sizes were slightly increased after the displacement reaction from the TEM images in Fig. 4(b–d). The average size for the Ru@Pt nanoparticles of pH 1, pH 2.2, and pH 8 was 4, 3.8, and 4.6 nm, respectively. However, their morphologies were similar to that of Fig. 4(a). This minute variation in sizes between each group suggested that the Ru nanoparticles were stable in various environments against corrosive dissolution. This behavior was not unexpected as Pourbaix diagram predicted similar behaviors. In addition, due to the coulombic balance during the displacement reaction, the loss of Ru introduces deposition of Pt that rendered the Ru@Pt at similar sizes. Moreover, results from EDX, listed in Table 1, confirmed the presence of Pt after the displacement reaction. The bath of pH 1 revealed the largest amount of Pt, followed by pH 2.2 and pH 8, indicating that the acidic environment was favored for Pt deposition or adsorption. These results were consistent with the XRD patterns in Fig. 3(b) since at pH 1 and pH 2.2, some of the Pt were alloyed with Ru so a relatively larger amount of Pt was reasonably expected.

**Table 1**
EDX results on Ru@Pt/XC72 from group A of pH 1, pH 2.2, and pH 8.

| | Pt (at%) | Ru (at%) |
|---|---|---|
| pH 1 | 11.08 | 88.92 |
| pH 2.2 | 6.65 | 93.35 |
| pH 8 | 3.38 | 96.62 |

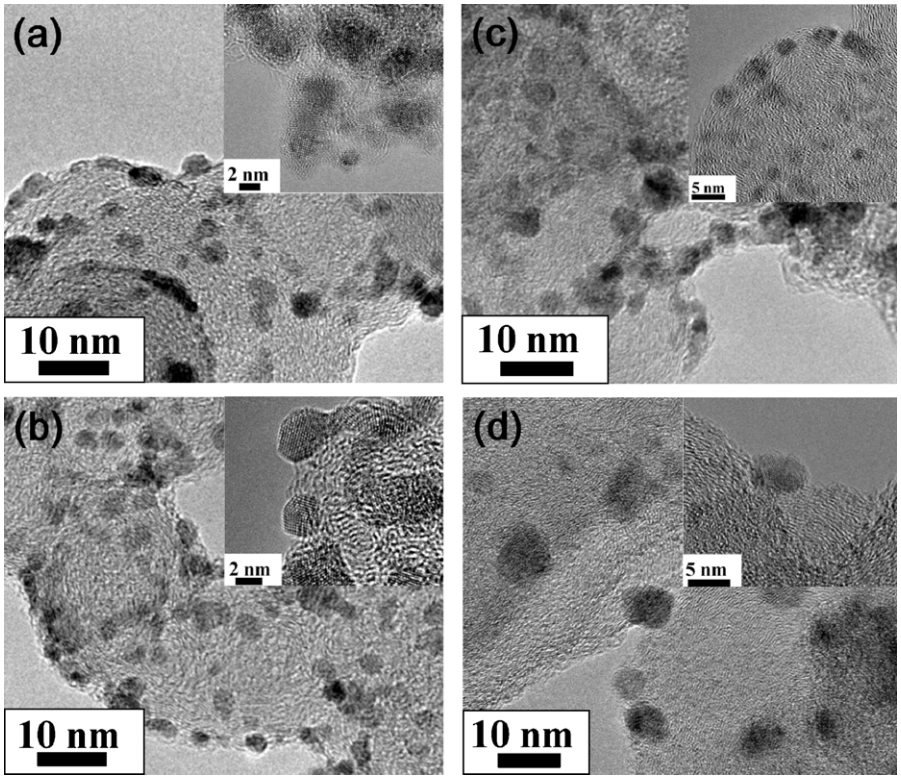


**Fig. 4.** The TEM images for (a) Ru/XC72 and Ru@Pt/XC72/CC from group A of (b) pH 1, (c) pH 2.2, and (d) pH 8. The insets are their respective images in high resolution.

**Table 2**
ICP-MS results on Ru@Pt/XC72/CC from group A of pH 1, pH 2.2, and pH 8, as well as their corresponding $H_2PtCl_6$ solution.

| | | Pt (μmol) | Ru (μmol) |
|---|---|---|---|
| Ru@Pt/XC72/CC | pH 1 | 1.26 | 2.02 |
| | pH 2.2 | 1.17 | 2.94 |
| | pH 8 | 0.62 | 4.86 |
| $H_2PtCl_6$ solution | pH 1 | 20.01 | 1.88 |
| | pH 2.2 | 21.61 | 1.37 |
| | pH 8 | 22.57 | 0.05 |

Since the EDX results provided qualitative evidences at best, more accurate determination for the Pt and Ru amount after the displacement reaction was obtained via ICP-MS. Table 2 presents the ICP-MS results for the Ru@Pt/XC72 from group A of pH 1, pH 2.2, and pH 8, as well as their corresponding $H_2PtCl_6$ solution after the displacement reaction. As listed, the Pt loading was 1.26, 1.17, and 0.62 μmol for samples of pH 1, pH 2.2, and pH 8, respectively. Apparently, a lower pH bath allowed more Pt deposition or adsorption on the remaining Ru nanoparticles, a behavior consistent with EDX results in Table 1. Likewise, the Ru loading was 2.02, 2.94, and 4.86 μmol for samples of pH 1, pH 2.2, and pH 8, respectively. For the corresponding $H_2PtCl_6$ solution, the amount of residual Pt at various pH values agreed well with what we expected. In addition, the amount of Ru cations in the $H_2PtCl_6$ solution was proportional to the Ru loss in Ru@Pt nanoparticles. Obviously, considerable Ru dissolution in conjunction with Pt deposition was observed at a low pH bath. From Table 2, the compositions for the Ru@Pt nanoparticles were $Pt_{38}Ru_{62}$, $Pt_{28}Ru_{72}$, and $Pt_{11}Ru_{89}$ for samples of pH 1, pH 2.2, and pH 8, respectively.

In order to remove possible effect of Ru corrosion encountered in the acidic electrolyte, we also obtained ICP-MS results from samples of Ru/XC72/CC immersed in aqueous solution of pH 1, pH 7, and pH 8 (reference group). Since the Pt cations were not present in the solution, the amount of Ru recorded in the solution was caused entirely by corrosive dissolution instead of displacement reaction. The Ru amount in pH 1, pH 7, and pH 8 bath was 0.31, 0.01, and 0.03 μmol, respectively. It can be seen that the Ru suffered from moderate corrosion in pH 1 bath but became relatively stable in pH 2 and pH 8 bath. Nevertheless, the amount of corrosive dissolution of pH 1 bath was still insufficient to account for the Ru content reported in Table 2. According to the Pourbaix diagram, the Ru is expected to be in a metallic state at 0 V for bath of pH 1, pH 2, and pH 8. Hence, we concluded that the observed displacement reaction was not driven by the corrosive dissolution of Ru but initiated by the difference in the redox potentials between the Ru and Pt complexes at different pH baths. According to Brankovic et al. [30], the driving force *(ΔU)* for the displacement reaction is the potential difference between the $[PtCl_6]^{2-}$ reduction and Ru oxidation as shown in equations below.

$$\Delta U = \Delta E_{Pt/PtCl_6^{2-}} - \Delta E_{Ru^0/Ru_{oxidized}} > 0 \quad (1)$$

$$[PtCl_6]^{2-} + 4e^- = Pt^0 + 6Cl^- \quad (2)$$

$$(\Delta E[V] \sim 0.74 + 0.015 \log [PtCl_6]^{2-}) \quad (3)$$

$$Ru^0 + x(H_2O) = RuO_xH_y + (2x - y)H^+ + (2x - y)e^- \quad (4)$$

In addition, it is believed that the oxidative dissolution of Ru occurs at a potential more positive than the equilibrium potential of $Pt/[PtCl_6]^{2-}$ so it is unlikely to trigger the displacement reaction [43].

### 3.2. XANES and EXAFS analysis

Since the activity for Pt complexes and their associated redox potentials are determined by the nature and number of ligands, the solution pH value therefore becomes very critical because the hydrolysis of Pt complexes is highly pH-dependant. The nature and number of ligand complexing the Pt cation in the electrolyte, as well as the oxidation state for Pt and Ru in the Ru@Pt nanoparticles can be inferred from XANES and EXAFS analysis. The Ru K-edge XANES spectra for the reference group (Ru/XC72/CC in pH 1, pH 2, and pH 8 solution) are demonstrated in Fig. 5, along with Ru and $RuO_2$ serving as the reference. The metallic Ru is established to have a K-edge absorption around 22,117 eV and its position is shifted to higher energy in oxidized state, as confirmed by the $RuO_2$. Spectra from the Ru/XC72/CC after immersing in $HClO_4$ (pH 1), de-ionized water (pH 7), and KOH (pH 8) suggested that some of the Ru existed in oxidized forms and their oxidation states were rather similar. However, the exact oxidation state was still unknown but its value was estimated between 0 and +4 as indicated by the absorption edge between Ru and $RuO_2$. According to literature, the Ru was prone to form surface oxide and hydroxide when it was immersing in a liquid electrolyte. Hence, the presence of Ru in an oxidized state was not entirely unsupported [44].

Fig. 6 exhibits the Ru K-edge XANES spectra for samples from group A and group B, respectively. In general, their spectra were similar to those obtained in Fig. 5. Hence, we concluded that the oxidation state of Ru remained unchanged regardless the electrolyte they encountered was $HClO_4$, KOH, or $H_2PtCl_6$. However, after further exploration, as shown in the inset of Fig. 6, it was found that the Ru from group A was slightly more oxidized than that in group B. This behavior was not unexpected as the samples from group B underwent a hydrogen reduction treatment leading to their reduced oxidized state. It is noted that from XRD in Figs. 2 and 3, the samples from group A and group B did not reveal the presence of $RuO_x$ or $Ru(OH)_x$. However, in the XANES spectra, the Ru existed in an oxidized state. We attributed this discrepancy to the sensitivity of XANES that took into consideration of both metallic Ru at the core and oxidized Ru on the surface. Besides, the oxidized Ru was likely amorphous that obscured the XRD signal.

Similarity in Figs. 5 and 6 confirmed that the Ru maintained an identical oxidation state with or without displacement reaction. Therefore, during displacement reaction, we believed that the oxidized Ru left the surface in the form of dissolved complexes and freshly exposed Ru adopted a similar oxidation state. To validate

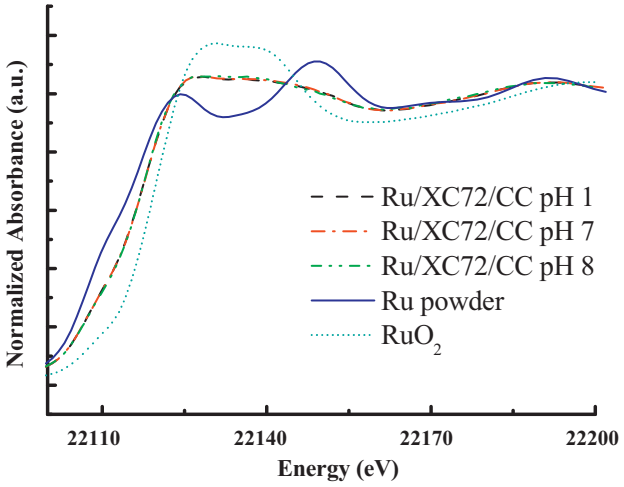


**Fig. 5.** The Ru K-edge XANES spectra of Ru, $RuO_2$, and Ru/XC72/CC from reference group of pH 1, pH 7, and pH 8.

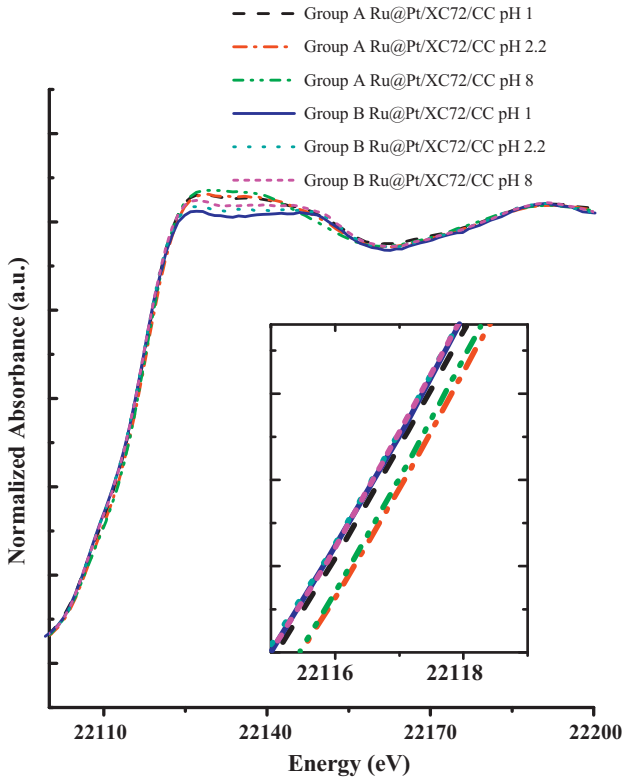


**Fig. 6.** The Ru K-edge XANES spectra of Ru@Pt/XC72/CC from group A and group B.

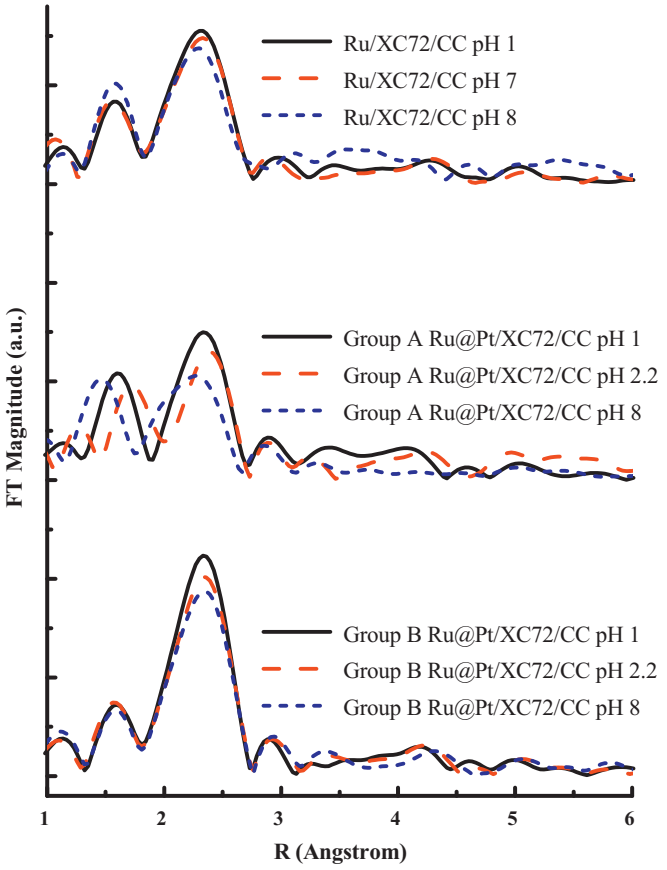


**Fig. 7.** The Ru K-edge Fourier-transformed EXAFS spectra from Figs. 5 and 6.

our premise, it is necessary to carry out XANES analysis on the electrolyte to verify the identity of dissolved Ru cations. Unfortunately, the Ru cations in the electrolyte after displacement reaction were so dilute that determination of their identity became rather difficult. From samples of group B, the oxidation state for Ru was not completely reduced to metallic form which suggested that the oxidized Ru state we observed was intrinsic to Ru after the Ru was exposed to electrolyte or ambient moisture.

The Ru K-edge Fourier-transformed EXAFS spectra for the reference group, group A, and group B are provided in Fig. 7. The peaks at 1.6 Å and 2.3 Å (without phase correction) were associated with Ru--O bond and Ru--Ru bond at the first shell coordination. The EXAFS fitting results are summarized in Table 3. For the reference group, the coordination number for Ru--O in all baths was around 2. This bonding between Ru and O was attributed to the formation of oxide or hydroxide on the Ru surface. On the other hand, the Ru--Ru coordination number was around 4–5, which was expected because earlier studies by Hwang et al. reported a similar coordination number for the Ru nanoparticles [24]. For the Ru@Pt/XC72/CC (sample of group A), we obtained a reduced Ru--O coordination number for pH 1 and pH 2.2 bath. On the other hand, the coordination number of Ru--Ru remained unchanged suggesting that the Ru core was likely intact. However, the EXAFS fitting did not reveal any Ru--Pt bond which excluded the possibility of Pt sitting next to Ru in the Ru@Pt nanoparticles. Nevertheless, once the hydrogen reduction treatment was performed (as shown in group B), the Ru--Pt coordination number of 1.33, 1.08, and 0.82 was obtained for pH 1, pH 2.2, and pH 8 bath, respectively. At the same time, the number of Ru--O bond became smaller due to the hydrogen reduction treatment. Likewise, the Ru--Ru bond remained relatively unchanged because the Ru core was mostly unaffected. According to Hu et al. [45], the Ru might establish a Ru--O-Ru bonding near its surface. In our case, the bridged oxygen was likely to connect both Pt and Ru forming a Ru--O-Pt on the surface of Ru nanoparticles. Hence, it became reasonable that the Ru--Pt coordination was observed as long as the bridged oxygen was removed during hydrogen reduction treatment.

In situ XAS measurements for the deposited Pt during displacement reaction was unlikely because there were excess Pt cations in the $H_2PtCl_6$ solution that provided strong background signals. Hence, it became rather challenging to detect any variation in the oxidation states for the deposited Pt cations on the electrode with presence of $H_2PtCl_6$ solution nearby. Fig. 8 demonstrates the Pt $L_{III}$-edge XANES spectra from $H_2PtCl_6$ solution at pH 1, pH 2.2, and pH 8, respectively. Also shown is the XANES for Pt foil. The purpose for this measurement is to determine the nature of complexing ions for the Pt cations in different environments. From literature, electronic transitions from $2p_{3/2}$ to 5d is responsible for the Pt $L_{III}$-edge which is also known as white line [46,47]. In general, the white line intensity is able to provide information on the oxidation state of Pt due to its relevance to the d-band vacancy. A larger white line intensity often infers more vacant d-band orbitals. From the XANES spectra, there appeared a high intensity white line for the Pt cations in $H_2PtCl_6$ solution at various pH values. These patterns were expected as the Pt cations were possibly present in $Pt^{4+}$. For the white line of Pt foil, its low intensity confirmed its metallic nature and its magnitude corresponded to the oxidation state of "0".

For the identity of Pt atoms which were deposited onto Ru after the displacement reaction, the Pt $L_{III}$-edge XANES spectra in Fig. 9 can provide insightful information. In general, for samples from group A and group B, the XANES spectra clearly demonstrated a notable distinction in which signals from group A revealed a larger d-band vacancy than those from group B. This trend was expected as samples from group B underwent a hydrogen reduction treatment. For samples of group A, obviously the pH 8 sample revealed

**Table 3**
EXAFS fitting parameters at the Ru K-edge for Ru/XC72/CC and Ru@Pt/XC72/CC under various conditions.

| | | Path | Coordination number, $N$ | Bond distance, $R$ (Å) | Inner potential shift, $\Delta E_0$ (eV) | Debye–Waller factor, $\Delta\sigma_j^2$ ($\times 10^{-3}$ Å$^2$) |
|---|---|---|---|---|---|---|
| Reference | pH 1 | Ru–O | 1.95 | 2.04 | −5.45 | 5.43 |
| | | Ru–Ru | 4.61 | 2.67 | −9.92 | 7.29 |
| | pH 7 | Ru–-O | 1.99 | 2.04 | −4.36 | 5.41 |
| | | Ru–-Ru | 5.00 | 2.67 | −10.4 | 7.98 |
| | pH 8 | Ru–-O | 1.94 | 2.04 | −6.15 | 3.32 |
| | | Ru–-Ru | 4.15 | 2.67 | −12.05 | 7.45 |
| Group A | pH 1 | Ru–-O | 1.23 | 2.05 | −0.55 | 0.13 |
| | | Ru–-Ru | 4.06 | 2.67 | −7.35 | 7.02 |
| | pH 2.2 | Ru–-O | 1.33 | 2.07 | −1.56 | 0.46 |
| | | Ru–-Ru | 4.28 | 2.68 | −7.10 | 8.26 |
| | pH 8 | Ru–-O | 1.99 | 2.02 | −7.46 | 1.78 |
| | | Ru–-Ru | 4.08 | 2.65 | −12.88 | 7.03 |
| Group B | pH 1 | Ru–-O | 1.07 | 2.05 | −6.54 | 4.23 |
| | | Ru–-Ru | 5.24 | 2.69 | −3.71 | 6.70 |
| | | Ru–-Pt | 1.33 | 2.71 | −9.44 | 5.91 |
| | pH 2.2 | Ru–-O | 1.36 | 2.05 | −5.03 | 5.30 |
| | | Ru–-Ru | 5.12 | 2.69 | −4.14 | 7.20 |
| | | Ru–-Pt | 1.08 | 2.70 | −13.59 | 6.62 |
| | pH 8 | Ru–-O | 1.41 | 2.05 | −0.47 | 6.96 |
| | | Ru–-Ru | 4.54 | 2.69 | −3.62 | 6.91 |
| | | Ru–-Pt | 0.82 | 2.71 | −8.24 | 5.64 |

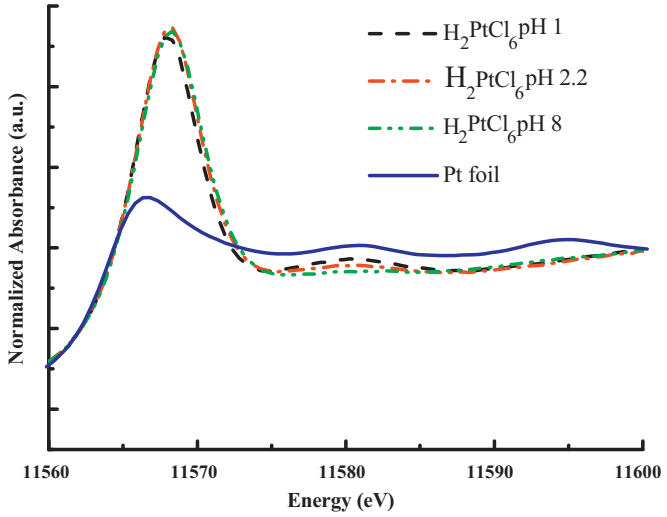


**Fig. 8.** The Pt $L_{III}$-edge XANES spectra of Pt foil and $H_2PtCl_6$ solution of pH 1, pH 2.2, and pH 8.

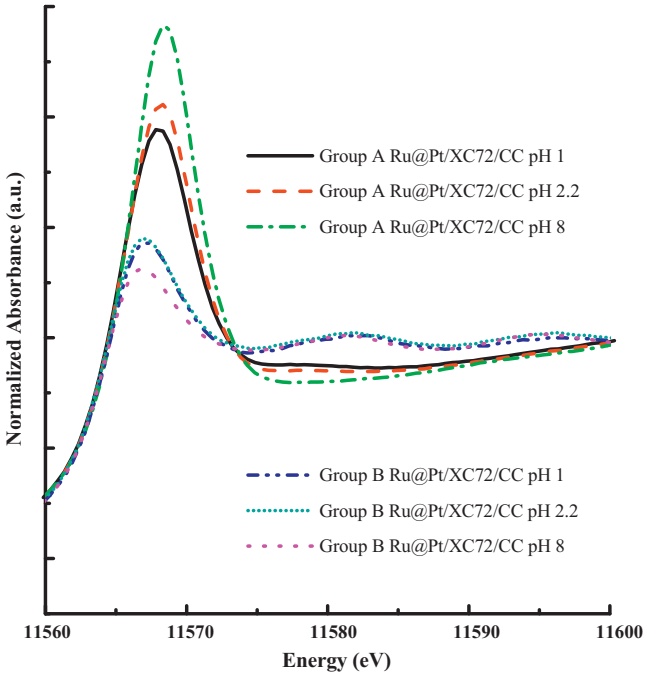


**Fig. 9.** The Pt $L_{III}$-edge XANES spectra of Ru@Pt/XC72/CC from group A and group B.

the largest d-band vacancy with its magnitude close to the $H_2PtCl_6$ solution in Fig. 8. This suggested that the Pt existed in +4 oxidation state on the Ru particle after the displacement reaction which inferred a physical adsorption process without involving the oxidation loss of Ru. In addition, for baths of pH 1 and pH 2, it appeared that the Pt still existed in the oxidized state albeit with a slightly reduced state. This trend was reversed from samples of group B in which the pH 8 sample demonstrated the lowest oxidative state with magnitude close to the metallic Pt foil shown in Fig. 8. However, the samples from pH 1 and pH 2.2 indicated that the Pt was still present at a slightly oxidized state. We surmised that at pH 8 the Pt atoms clustered around themselves revealing a metallic behavior while at pH 1 and pH 2.2, the Pt atoms were intermixed with Ru forming a quasi-alloying state instead. Earlier, it was suggested by Sasaki et al. that in alloying of PtRu the Pt exhibits a larger d-band vacancy because its electronic structure is influenced by nearby Ru [17]. This might be one of the reasons accountable for the recorded oxidized Pt in Fig. 9. An alternative explanation is that the $RuO_x$ is able to withdraw electrons partially from the Pt nearby leading to relatively stronger white line intensities.

The Fourier-transformed EXAFS spectra for $H_2PtCl_6$, group A, and group B are exhibited in Fig. 10. As shown, the peaks at 1.7 Å and 2.0 Å (without phase correction) were associated with the Pt–O bond and Pt–Cl bond at the first shell coordination, respectively. On the other hand, the peaks at 2.1 Å and 2.7 Å (without phase correction) corresponded to the Pt–Ru bond and Pt–Pt bond at the first shell coordination, respectively. The EXAFS fitting results are summarized in Table 4. In $H_2PtCl_6$ solution, the coordination number of Pt–O was 1.31, 1.65, and 3.58 for pH 1, pH 2.2, and pH 8 bath, respectively. In addition, the EXAFS results determined that the coordination number of Pt–Cl was 4.69, 4.35, and 2.42 for pH 1, pH 2.2, and pH 8 bath, respectively. Previously, Spieker et al., in their careful study of dilute $H_2PtCl_6$ acids with various pH values, observed that the chloride ion ligands associated with the Pt complexes can be exchanged by hydroxide ligand (OH) or aquo ligand ($OH_2$) due to the hydrolysis reaction [33]. Similar phenomena

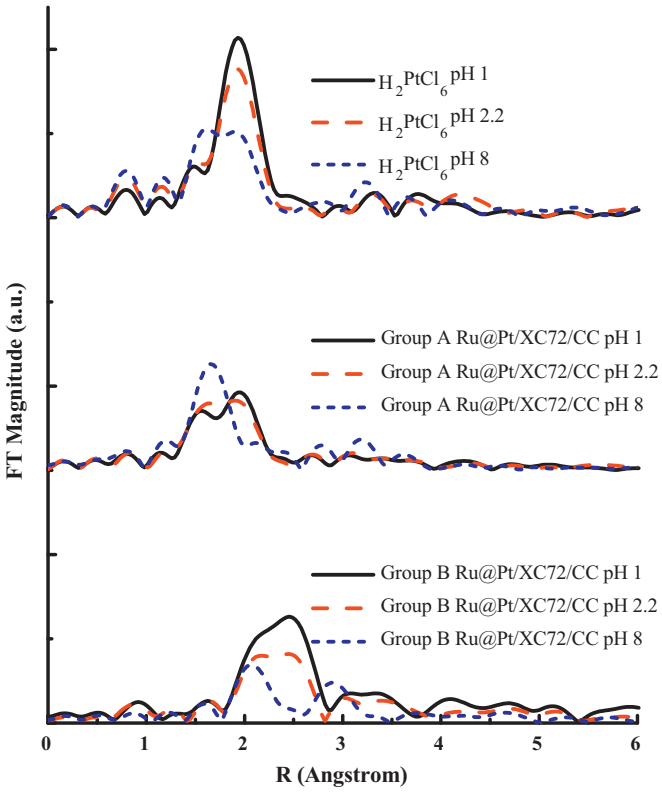


**Fig. 10.** The Pt $L_{III}$-edge Fourier-transformed EXAFS spectra from Figs. 8 and 9.

were observed in this work in which the EXAFS fitting for samples of different pHs indicated a significant ligand changeup between the Pt–Cl and Pt–O. In other words, the number of chloride ligands on the Pt complexes was reduced due to the hydrolysis reaction when the pH value was increased. The variation of Pt ligand species was believed to be responsible for the notable difference toward the behavior of displacement reaction.

For group A, the sum of coordination number for Pt–O and Pt–Cl was decreased after the deposition/attachment to the Ru. This indicated that some of the ligands were removed from the Pt complexes when the Pt cations were anchored to Ru. Nevertheless, a direct Pt–Ru bond was not established which was consistent with what we found in Table 4. Therefore, the bridged oxygen structure was believed to be the linkage between the Pt and Ru. For samples in group B, the coordination environment was changed dramatically with the disappearance of Pt–O and Pt–Cl. Instead, we witnessed the formation of Pt–Ru and Pt–Pt. The coordination number for Pt–Ru was 5.75, 4.23, and 3.21 for pH 1, pH 2.2, and pH 8 bath. These results suggested that at low pH value, the Pt atoms were embedded in the Ru core occupying lattice sites vacated by dissolving Ru atoms. At a high pH value, the Pt cations were merely adsorbed physically on the Ru surface which led to a decrease in the Pt–Ru coordination number after the hydrogen reduction treatment. On the other hand, the coordination number for Pt–Pt was 1.71, 2.43, and 4.24 for pH 1, pH 2.2, and pH 8 bath, respectively. At a low pH value, the Pt atoms were assumed to mix with Ru forming a quasi-alloying state that resulted in a small Pt–Pt coordination number. On the contrary, the Pt clusters on the Ru surface were expected to exist for the pH 8 bath. These results were consistent with XRD data in Fig. 3, leading to a larger Pt–Pt coordination number. The reason that Pt continued to substitute the Ru atoms in the beneath layers is because the Ru nanoparticles suffered from severe oxidation dissolution in an acidic electrolyte as compared to that of alkaline electrolyte. This behavior can be confirmed from Table 2 in which a significantly larger Ru amount (1.88 μmol) was found in the $H_2PtCl_6$ solution of pH 1. In contrast, a moderate amount of Ru (0.05 μmol) was recorded in the $H_2PtCl_6$ solution of pH 8. We rationalized that the oxidative dissolution of Ru nanoparticles produced sufficient porosity that allowed the deposition of Pt cations underneath the Ru surface.

By summarizing the analytical results from XRD, ICP-MS, TEM, EDX, and XAS spectra, a mechanism for the Pt displacement reaction on the Ru nanoparticles is provided in the schematic diagrams shown in Fig. 11. Fig. 11(a) depicts the scenario for pH 1 and pH 2 in which the Pt cations were partially reduced accompanied by the oxidative dissolution of Ru on the surface. The dissolution of Ru was resulted from Pt reduction. Meanwhile, the formation of Ru oxide layer on the surface took place slowly during the Ru immersion into aqueous baths which eventually terminated the displacement reaction as the surface oxide layer prevented the underneath Ru from further dissolving and consequently inhibiting the reduction of Pt ions. Fig. 11(b) illustrates the mechanism of PtRu displacement reaction in pH 8 scenario. The Pt cations were physically adsorbed on the Ru surface mostly, and after the hydrogen reduction treatment, the Pt cations were reduced and agglomerated as clusters on the Ru surface. In short, the pH values of $H_2PtCl_6$ acid played a critical role for the severity of displacement reaction between the Pt and Ru and its resulting alloy state.

**Table 4**
EXAFS fitting parameters at the Pt $L_{III}$-edge for Ru/XC72/CC and Ru@Pt/XC72/CC under various conditions.

| | | Path | Coordination number, $N$ | Bond distance, $R$ (Å) | Inner potential shift, $\Delta E_0$ (eV) | Debye–Waller factor, $\Delta\sigma_j^2$ ($\times 10^{-3}$ Å$^2$) |
|---|---|---|---|---|---|---|
| $H_2PtCl_6$ solution | pH 1 | Pt–O | 1.31 | 1.99 | −2.14 | 2.79 |
| | | Pt–Cl | 4.69 | 2.31 | 10.16 | 2.79 |
| | pH 2.2 | Pt–O | 1.65 | 1.99 | −1.95 | 3.77 |
| | | Pt–Cl | 4.35 | 2.31 | 10.34 | 3.77 |
| | pH 8 | Pt–O | 3.58 | 1.99 | 1.44 | 4.21 |
| | | Pt–Cl | 2.42 | 2.31 | 13.83 | 4.21 |
| Group A | pH 1 | Pt–O | 1.95 | 1.99 | 7.26 | 1.78 |
| | | Pt–Cl | 1.69 | 2.30 | 9.16 | 1.57 |
| | pH 2.2 | Pt–O | 1.83 | 2.00 | 7.79 | 1.79 |
| | | Pt–Cl | 2.41 | 2.30 | 8.80 | 4.47 |
| | pH 8 | Pt–O | 3.66 | 1.99 | 3.73 | 2.42 |
| | | Pt–Cl | 1.83 | 2.32 | 18.35 | 11.17 |
| Group B | pH 1 | Pt–Ru | 5.75 | 2.71 | 8.66 | 5.61 |
| | | Pt–Pt | 1.71 | 2.76 | 7.52 | 2.96 |
| | pH 2.2 | Pt–Ru | 4.23 | 2.71 | 7.69 | 5.60 |
| | | Pt–Pt | 2.43 | 2.76 | 8.65 | 4.82 |
| | pH 8 | Pt–Ru | 3.21 | 2.71 | 6.69 | 6.25 |
| | | Pt–Pt | 4.24 | 2.75 | 7.26 | 4.66 |

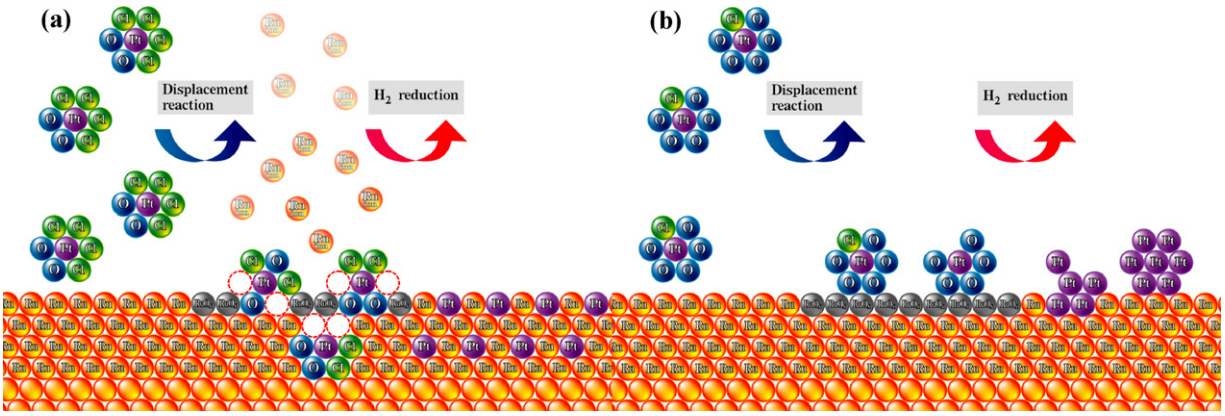


**Fig. 11.** Schematic diagrams for PtRu displacement reaction occurring at (a) low pH and (b) high pH conditions.

### 3.3. Electrochemical analysis of Ru@Pt/XC72/CC

An alternative route to validate the core–shell structure for the Ru@Pt nanoparticles is to carry out CO stripping measurements on the samples after hydrogen reduction treatment (group B). Since the CO is known to form a strong chemical bond with Pt that deactivates the Pt from subsequent electrochemical actions, the modification of Pt by underlying Ru has been reported to alleviate the CO poisoning effect via a mechanism of electronic modification [10,11]. As a result, the Ru@Pt nanoparticles are expected to reveal superior performances for CO oxidation and this can be easily seen by the negative shift of the onset potential in CO stripping profiles. To carry out the CO stripping experiments, we saturated 0.5 M $H_2SO_4$ solution with gases of 3 vol.% CO and 97 vol.% $N_2$ for 30 min at −0.15 V (vs. Ag/AgCl) to ensure adequate adsorption of CO on the Ru@Pt/XC72/CC. Afterward, cyclic voltammetric scans (CV) were imposed on the samples for −0.2–0.9 V to obtain current responses associated with CO oxidation. The resulting CV profiles are displayed in Fig. 12. Also shown for comparison is the commercial PtRu from E-TEK. The commercial product of E-TEK PtRu contained PtRu nanoparticles supported on the XC72 in 40 wt% and the PtRu atomic ratio was 1:1. In contrast, in our Group B samples, the PtRu compositions were $Pt_{11}Ru_{89}$, $Pt_7Ru_{93}$, and $Pt_3Ru_{97}$. The exact catalyst loadings for our samples were validated by thermogravimetric analysis (TGA) measurements in which carbon supports (XC72/CC) were deliberately burned off at elevated temperature, leaving metallic PtRu behind. For the E-TEK sample, the PtRu loading was 0.64 mg/cm$^2$. For Group B of pH 1, pH 2.2, and pH 8, we recorded PtRu loadings of 0.2, 0.24, and 0.53 mg/cm$^2$, respectively. These values were used in calculating the mass activities for these samples. As shown in Fig. 12, the E-TEK PtRu exhibited an onset potential of 0.23 V, while the Ru@Pt nanoparticles of pH 1, pH 2.2, and pH 8 displayed an onset potential of 0, 0.02, and 0.04 V, respectively. The improvements in the onset potentials for the CO stripping provided additional evidences of core–shell formation in our samples. In addition, the sample of pH 1 revealed the lowest onset potential because its surface structure was between alloyed and core–shell arrangement that revealed the largest ligand effect.

Tolerance for CO poisoning can also be confirmed by subjecting the Ru@Pt nanoparticles (group B) in mixed gas of $H_2/N_2/CO$ (200/9.7/0.3 in vol. ratio) for $H_2$ oxidation reaction. The experiments were performed at 0.05 V (vs. Ag/AgCl) in 0.5 M $H_2SO_4$ solution for 1 h to record the resulting current responses. Fig. 13 demonstrates the $H_2$ oxidation curves for both apparent current density and mass activities in which identical trends were observed. In general, the obtained current revealed moderate instability which was caused by gas bubble adsorption and desorption. These undesirable current fluctuations were also observed by Brankovic et al. and Adzic et al. [21,48]. For the E-TEK PtRu, there appeared a gradual loss in the $H_2$ oxidation ability which agreed with earlier results [21]. They attributed this degradation behavior to the CO poisoning of Pt. A similar pattern was also witnessed for Ru@Pt nanoparticles of pH 8 which was possibly due to the formation of Pt clusters on the Ru surface that exposed unalloyed Pt for Pt-CO bonding. In contrast, the Ru@Pt nanoparticles of pH 1 demon-

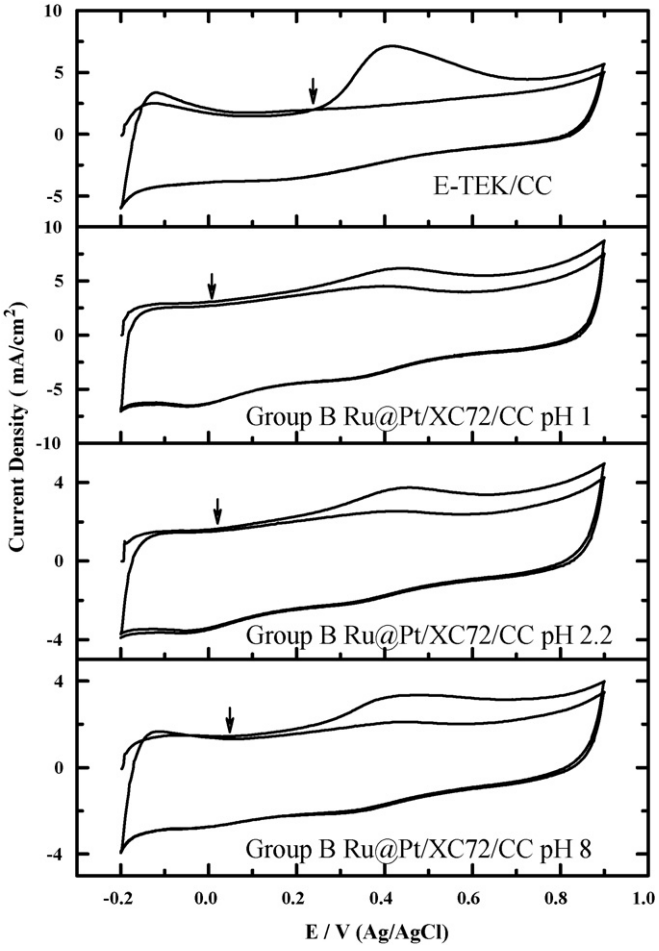


**Fig. 12.** The cyclic voltammetric curves for CO oxidation on E-TEK/CC and Ru@Pt/XC72/CC from group B of pH 1, pH 2.2, and pH 8.

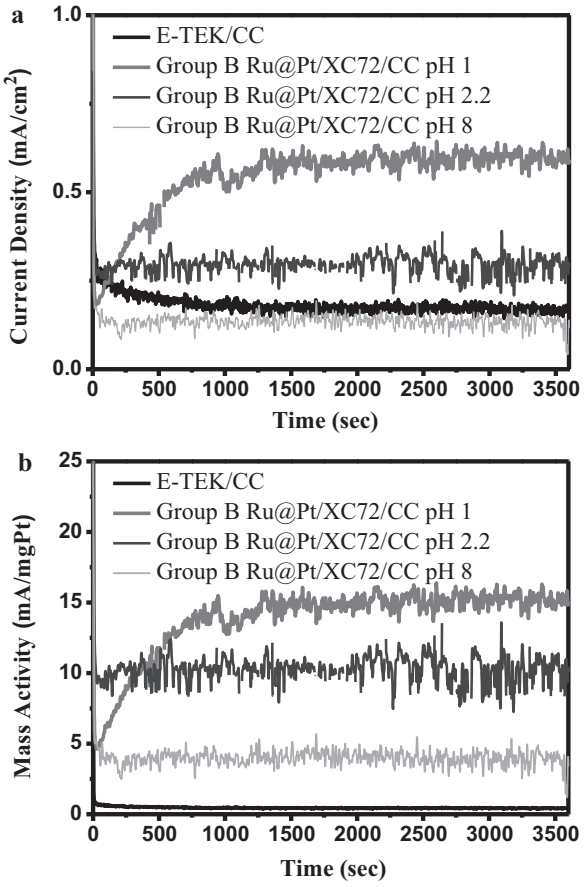


**Fig. 13.** The $H_2$ oxidation curves in (a) apparent current density and (b) mass activity on E-TEK/CC and Ru@Pt/XC72/CC from group B of pH 1, pH 2.2, and pH 8.

strated an increasing catalytic ability for $H_2$ oxidation initially but stabilized after 1000 s with negligible performance degradation. This notable improvement further substantiated the formation of desirable core–shell structure that enabled facile CO removal as evidenced in Fig. 12.

It is noted that the in situ XAS would be very insightful to detect any changeup in Pt or Ru during fuel cell operation when the electrode is under polarization. In a recent article by Zhou et al., they carried out the in situ XAS on $Pd_2Co$-supported Pt monolayer for the oxygen reduction reaction and observed that the white line intensity of the Pt $L_{III}$-edge did not show any noticeable change until the applied potential was positive of 0.9 V [49]. In our case, the potential for the hydrogen oxidation reaction occurred at 0.25 V so it is likely that the in situ XAS for the hydrogen oxidation reaction might not pick up sufficient variation in the white line intensity of Pt $L_{III}$-edge. However, there is also possibility that the Ru would become Ru oxide or hydroxide at 0.25 V and hence alters the electronic structure of Pt nearby. In such scenario, the Pt $L_{III}$ white line might be slightly affected.

## 4. Conclusion

The mechanism of Pt displacement reaction on the Ru to form Ru@Pt nanoparticles was investigated by immersing the carbon-supported Ru nanoparticles in hexachloroplatinic acids with various pH values, followed by hydrogen reduction. XRD patterns demonstrated that the Ru hcp lattice was expanded slightly after Pt incorporation. Results from ICP-MS suggested that the dissolution of Ru was mostly caused by the reduction of Pt cations. TEM images demonstrated a uniform distribution of Ru@Pt in size of 3–5 nm. Analysis from XANES and EXAFS indicated that the pH value of hexachloroplatinic acids determined the type of ligands around the Pt cations that led to different states of PtRu upon displacement reaction. After hydrogen reduction, samples from pH 1 bath revealed a desirable core–shell structure that displayed a reduced onset potential in CO stripping measurements and stable catalytic performance for $H_2$ oxidation with negligible performance degradation.

## Acknowledgements

The authors are grateful to Professor Pang Lin and Professor George Tu for their kind assistance with the laboratory equipment. Financial supports from National Science Council of Taiwan (NSC-98-2221-E-009-040-MY2) and National Synchrotron Radiation Center (2009-2-063-1) are noted.

## References

[1] K.R. Lee, M.K. Jeon, S.I. Woo, Appl. Catal. B-Environ. 91 (2009) 428–433.
[2] F.H.B. Lima, E.R. Gonzalez, Appl. Catal. B-Environ. 79 (2008) 341–346.
[3] S.H. Oh, R.M. Sinkevitch, J. Catal. 142 (1993) 254–262.
[4] A. Manasilp, E. Gulari, Appl. Catal. B-Environ. 37 (2002) 17–25.
[5] P. Justin, P. Hari Krishna Charan, G. Ranga Rao, Appl. Catal. B-Environ. 100 (2010) 510–515.
[6] S. Garcia-Rodriguez, F. Somodi, I. Borbath, J.L. Margitfalvi, M.A. Pena, J.L.G. Fierro, S. Rojas, Appl. Catal. B-Environ. 91 (2009) 83–91.
[7] D. Lim, D. Choi, W. Lee, H. Lee, Appl. Catal. B-Environ. 89 (2009) 484–493.
[8] H.J. Kim, S.M. Choi, S. Green, G.A. Tompsett, S.H. Lee, G.W. Huber, W.B. Kim, Appl. Catal. B-Environ. 101 (2011) 366–375.
[9] S. Desai, M. Neurock, Electrochim. Acta 48 (2003) 3759–3773.
[10] P. Waszczuk, G.Q. Lu, A. Wieckowski, C. Lu, C. Rice, R.I. Masel, Electrochim. Acta 47 (2002) 3637–3652.
[11] T. Yajima, H. Uchida, M. Watanabe, J. Phys. Chem. B 108 (2004) 2654–2659.
[12] M.S. Nashner, A.I. Frenkel, D. Somerville, C.W. Hills, J.R. Shapley, R.G. Nuzzo, J. Am. Chem. Soc. 120 (1998) 8093–8101.
[13] H. Nitani, T. Nakagawa, H. Daimon, Y. Kurobe, T. Ono, Y. Honda, A. Koizumi, S. Seino, T.A. Yamamoto, Appl. Catal. A-Gen. 326 (2007) 194–201.
[14] S. Alayoglu, A.U. Nilekar, M. Mavrikakis, B. Eichhorn, Nat. Mater. 7 (2008) 333–338.
[15] S.Y. Huang, S.M. Chang, C.L. Lin, C.H. Chen, C.T. Yeh, J. Phys. Chem. B 110 (2006) 23300–23305.
[16] B.D. McNicol, R.T. Short, J. Electroanal. Chem. 81 (1977) 249–260.
[17] K. Sasaki, J.X. Wang, M. Balasubramanian, J. McBreen, F. Uribe, R.R. Adzic, Electrochim. Acta 49 (2004) 3873–3877.
[18] Y.J. Ando, K. Sasaki, R. Adzic, Electrochem. Commun. 11 (2009) 1135–1138.
[19] R.F. Wang, H. Li, H.Q. Feng, H. Wang, Z.Q. Lei, J. Power Sources 195 (2010) 1099–1102.
[20] H.B. Zhao, L. Li, J. Yang, Y.M. Zhang, Electrochem. Commun. 10 (2008) 1527–1529.
[21] S.R. Brankovic, J.X. Wang, R.R. Adzic, Electrochem. Solid-State Lett. 4 (2001) A217–A220.
[22] E. Spinace, A.O. Neto, M. Linardi, J. Power Sources 129 (2004) 121–126.
[23] C.H. Chen, L.S. Sarma, D.Y. Wang, F.J. Lai, C.C. Al Andra, S.H. Chang, D.G. Liu, C.C. Chen, J.F. Lee, B.J. Hwang, ChemCatChem 2 (2010) 159–166.
[24] B.J. Hwang, L.S. Sarma, C.H. Chen, C. Bock, F.J. Lai, S.H. Chang, S.C. Yen, D.G. Liu, H.S. Sheu, J.F. Lee, J. Phys. Chem. C 112 (2008) 19922–19929.
[25] S.T. Kuk, A. Wieckowski, J. Power Sources 141 (2005) 1–7.
[26] S. Roy, M. Matlosz, D. Landolt, J. Electrochem. Soc. 141 (1994) 1509–1517.
[27] L.A. Porter, H.C. Choi, A.E. Ribbe, J.M. Buriak, Nano Lett. 2 (2002) 1067–1071.
[28] L. Magagnin, R. Maboudian, C. Carraro, J. Phys. Chem. B 106 (2002) 401–407.
[29] S. Manandhar, J.A. Kelber, Electrochim. Acta 52 (2007) 5010–5017.
[30] S.R. Brankovic, J. McBreen, R.R. Adzic, J. Electroanal. Chem. 503 (2001) 99–104.
[31] S.R. Brankovic, J.X. Wang, Y. Zhu, R. Sabatini, J. McBreen, R.R. Adzic, J. Electroanal. Chem. 524 (2002) 231–241.
[32] Y.C. Hsieh, P.W. Wu, Y.J. Lu, Y.M. Chang, J. Electrochem. Soc. 156 (2009) B735–B742.
[33] W.A. Spieker, J. Liu, J.T. Miller, A.J. Kropf, J.R. Regalbuto, Appl. Catal. A-General 232 (2002) 219–235.
[34] G.X. Zhang, S.H. Sun, D.Q. Yang, J.P. Dodelet, E. Sacher, Carbon 46 (2008) 196–205.
[35] M. Newville, J. Synchrotron Radiat. 8 (2001) 322–324.
[36] B. Ravel, M. Newville, J. Synchrotron Radiat. 12 (2005) 537–541.
[37] H.Y. Lee, T.B. Wu, J.F. Lee, J. Appl. Phys. 80 (1996) 2175–2180.
[38] J.J. Rehr, R.C. Albers, Rev. Modern Phys. 72 (2000) 621–654.
[39] E. Antolini, Appl. Catal. B-Environ. 88 (2009) 1–24.
[40] K.W. Park, Y.E. Sung, S. Han, Y. Yun, T. Hyeon, J. Phys. Chem. B 108 (2004) 939–944.

[41] D.S. Yuan, S.Z. Tan, Y.L. Liu, J.H. Zeng, F.P. Hu, X. Wang, P.K. Shen, Carbon 46 (2008) 531–536.
[42] S. Song, Y. Liang, Z. Li, Y. Wang, R. Fu, D. Wu, P. Tsiakaras, Appl. Catal. B-Environ. 98 (2010) 132–137.
[43] D. Michell, D.A.J. Rand, R. Woods, J. Electroanal. Chem. 89 (1978) 11–27.
[44] Y. Sugawara, A.P. Yadav, A. Nishikata, T. Tsuru, J. Electrochem. Soc. 155 (2008) B897–B902.
[45] C.C. Hu, H.R. Chiang, C.C. Wang, J. Solid-State Electrochem. 7 (2003) 477–484.
[46] P.H. Citrin, G.K. Wertheim, Phys. Rev. B 27 (1983) 3176–3200.
[47] G. Meitzner, G.H. Via, F.W. Lytle, J.H. Sinfelt, J. Phys. Chem. 96 (1992) 4960–4964.
[48] R.R. Adzic, J. Zhang, K. Sasaki, M.B. Vukmirovic, M. Shao, J.X. Wang, A.U. Nilekar, M. Mavrikakis, J.A. Valerio, F. Uribe, Top Catal. 46 (2007) 249–262.
[49] W.P. Zhou, K. Sasaki, D. Su, Y. Zhu, J.X. Wang, R.R. Adzic, J. Phys. Chem. C 114 (2010) 8950–8957.